

Chapter 2

Theoretical Concepts of Scanning Probe Microscopy and Dynamic Light Scattering and Their Relation to the Study of Peptide Nanostructures

Abstract This chapter details the physical theoretical concepts and relevant background knowledge for the SPM techniques, alongside others such as DLS. Current understanding of the nanostructure of the amyloid peptide which has been the focus of this work, A β , is also detailed, gathering together information from a variety of experimental techniques. It is the aim of this chapter, and the one that follows it to provide a solid understanding of the work conducted within this thesis, and its relevance to Alzheimer's disease and the aggregation of A β .

2.1 Introduction

In order to study any biological material on the nanoscale one requires the correct tool to do so. There are several methods which can allow the study of protein morphology at this level but perhaps the most common and versatile is Scanning Probe Microscopy (SPM). Originally developed in 1982 as Scanning Tunnelling Microscopy (STM) the technique quickly evolved into the type of SPM focused on in this work, Atomic Force Microscopy [1–3]. The use of AFM for the high resolution imaging of materials surfaces has become increasingly common place in a wide range of subject areas, including biosciences and engineering [4]. Recent technological advancements make it possible to learn more about a sample than just its topography, and properties such as chemical composition, nanomechanics, thermal conductivity, elasticity and the Young's Modulus can all be determined [5–13]. The aim of this PhD has been to apply more well known, and also bespoke, AFM methods to the peptide Amyloid beta 1:42 (A β 1:42), the main pathogenic component of Alzheimer's disease (AD), with the hope of elucidating more about its nanostructure, assembly, dynamics and interaction with potential pharmaceuticals.

This first chapter focuses on the theoretical concepts and current literature relevant to the work in this thesis. The first section is devoted to the theoretical concepts which govern AFM, and the other techniques used in this work. The chapter which follows is a review of the A β 1:42 and its role in AD, and the biological process in which amyloid peptides gain their toxicity.

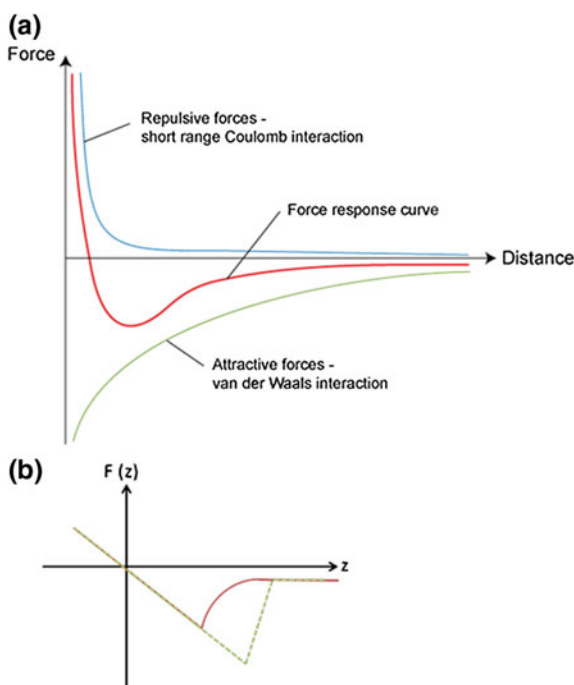
2.2 Scanning Probe Microscopy

Some SPM techniques, including AFM, are capable of examining the surface properties of a sample ultimately with atomic resolution, but typically of a few nanometers (nm), whilst generating 3D images of the sample in questions. In general a probe, with a tip radius of approximately 5–10 nm, is scanned across the sample surface in a raster pattern. The interaction between the tip and the sample is used to generate the 3D image map, and allow determination of topological, nanomechanical or spectroscopical data. The tip-surface interactions are an essential component of AFM, and will first be discussed in detail below.

2.2.1 Tip-Surface Interactions

The tip-surface interaction can have a strong effect on cantilever deflection, as AFM gathers information on the sample by sensing the force interactions between the tip and the surface. Close to the surface of the sample, Coulomb electron repulsions and van der Waals (VDW) forces dominate, while forces such as electrostatic and magnetic are more dominate at longer distances exceeding 1–10 nm (Fig. 2.1).

Fig. 2.1 **a** Showing the tip-surface interaction between a cantilever probe and sample. The force response curve is the response of the probe to the forces acting upon it and is shown in red © DoITPoMS, University of Cambridge [17] and **b** the approach-retract curve showing the path of the cantilever when governed by repulsive and attractive forces. The approach (*red*) and retract (*green*) are both shown



When the tip is far away (a few nm) from the sample surface the dominant force is attractive due to the VDW forces, and does not deflect. As the cantilever approaches this attractive VDW force increases in strength until the atoms are close enough for their electrons to interact and repel one another. As the attractive force increases, so does the total attractive force on the cantilever until dF/dz exceeds the spring constant of the cantilever and the tip snaps into contact with the sample surface. Once in contact the tip-surface interaction is governed by the repulsive regime due to Coulomb forces. Coulomb forces arise because of the electrostatic repulsion between the electron clouds of tip and sample. This repulsion becomes stronger the closer the tip is to the sample surface.

In addition to these attractive and repulsive forces, ambient AFM imaging must also contend with the thin layer of water which will cover the sample surface forming the meniscus. The meniscus gives rise to capillary forces between the sample and the tip, which is in most cases an adhesive force [14, 15].

Imaging in liquid presents a different challenge, as capillary forces are absent and VDW forces being significantly reduced [16]. Instead the tip-surface interaction is dominated by electrostatic forces. The charge of the sample being imaged is masked by that of the buffer solution being used for imaging due to the interactions between the co- and counter-ions it contains. This screening charge is known as the electric double layer and determines the resolution which can be achieved when imaging under-liquid as it determines the tip-sample distance [16]. The buffer must be finely tuned to minimise these electrostatic interactions by negating charged interactions.

On retraction the cantilever follows the same path as approach, but in reverse. Overcoming the meniscus attraction generates a notable negative deflection of the cantilever, which must be larger than the snap-in due to the initial approach, until the cantilever can overcome the attractive force and jump-off the sample surface.

Over the larger distances, longer range forces come into play to govern the interaction between the sample and the tip, and can be exploited by the use of conducting or magnetic cantilevers. A simplified equation can be used to explain the interactions between F_E , the electrostatic force, and F_M , the magnetic force:

$$F_E = -\frac{1}{2}(\Delta V)^2 \frac{\partial c}{\partial s}$$

$$F_M = \nabla(m \cdot B),$$

where C is the tip-surface capacitances, s the separation between tip and surface, ΔV the potential difference between sample and tip, m the tip's magnetic dipole and B the magnetic field from the sample [18]. These simplified equations give a feel for how tip surface interactions can be used to detect sample properties, but do not take into consideration the geometry, electrical, magnetic or structural properties of either the tip or the sample.

2.2.2 AFM Detection Modes

The SPM techniques covered here are all designed around the same system, in which samples are scanned in a raster pattern beneath a stationary probe with deflection of the force sensitive cantilever being continuously monitored. The sample movements are controlled by the scanner, upon which it is attached (by means of a magnetic “puck”) operating in the raster way along x-y axis. An alternative to this sample scanning method of AFM is probe scanning, where the sample is fixed and the probe is moved across the sample surface using a piezo to drive the movements as before. In sample scanning mode the mass of the sample itself must be included in the feedback loop and limiting the dimensions of the sample which can be imaged [19]. Probe scanning AFM’s do not have this limitation, and are often simpler for work which needs to be conducted under-liquid as it is easier to add the necessary accessories [19]. The construction of a probe scanning AFM is considerably more complex than a sample scanning one, and is also more susceptible to the introduction of vibrations during use, while sample scanning systems are simple and less susceptible to interference while scanning [19]. The scanner itself can come with a range of capabilities linked to scan size and lateral resolution. Typically work here used a large scale scanner as biological materials were not being studied on the atomic level. The specific AFM type used here, a Multi-Mode (Bruker, USA), is capable of numerous different detection systems. Those used in this work are detail more below.

Contact mode (CM) The topography is measured by moving the probe to scan the sample surface, and generating a feedback loop using the cantilevers deflection, which then allows details of the samples topography to be generated as a 3D image map. Onto the reverse of the cantilever a laser beam is focused, which is reflected onto a 4 quadrant photo-diode. Any vertical or horizontal change in behaviour of the cantilever alters the position of the laser on the photo-diode, (Figs. 2.2 and 2.3a). Upper and lower quadrants record changes in vertical height, generated by the topology of the sample directly, while lateral quadrants reflect friction or torsion based events on the cantilevers position. In CM the cantilever must be kept within the repulsive Coulomb force dominated regime until after the initial snap-into the sample surface. The feedback loop is used to maintain a tightly controlled position, or set point deflection, for the cantilever during scanning, using the addition of a z-axis piezo to adjust the height of the sample relative to the tip. By maintaining a constant deflection the force between the tip and the sample remains constant. Hooke’s law is used to calculate the force, F :

$$F = -kx,$$

where k is the spring constant of the cantilever and x is the cantilever deflection. CM is ideal for imaging any stable or hard samples that are not affected by interactions with the tip.

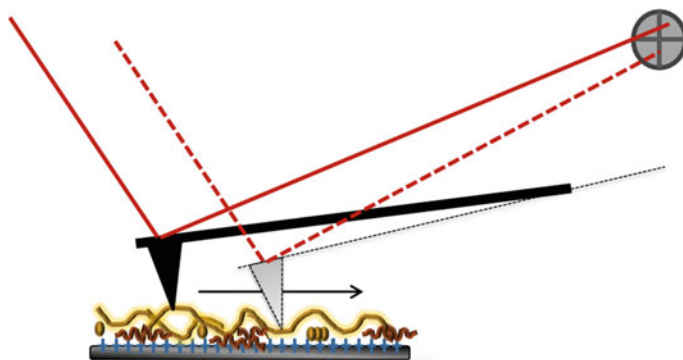


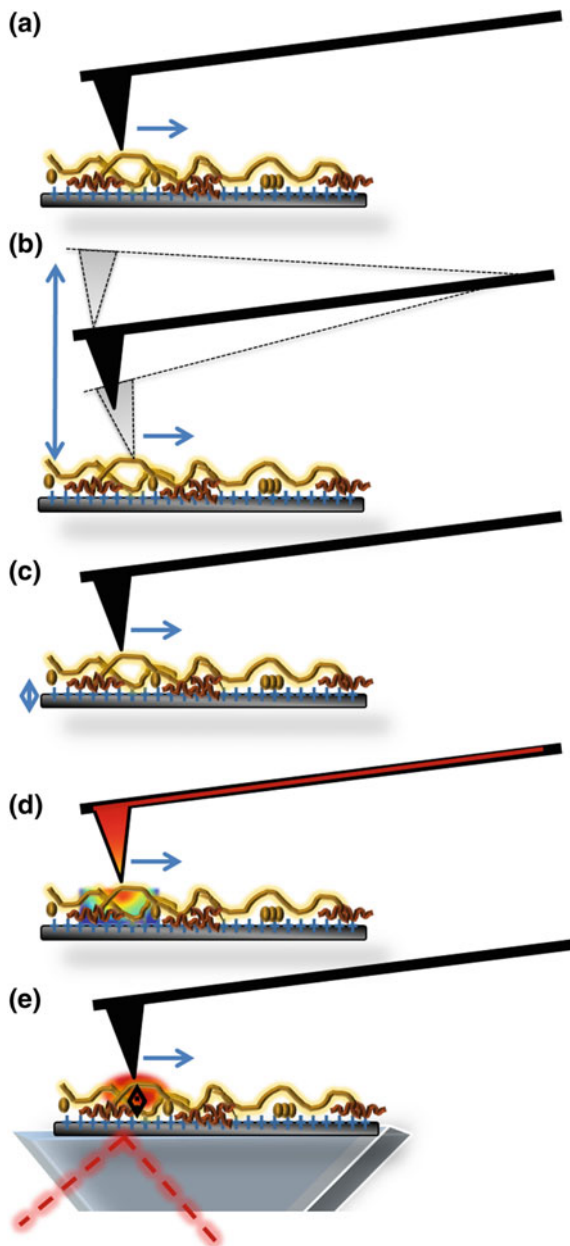
Fig. 2.2 A laser is focused onto the reverse of the cantilever, and deflected onto a four-quadrant photodiode. Any changes in topography as the cantilever scans in the x-y direction lead to the movement of the sample in the z direction. This change is reflected in a change in the deflection of the laser on the photodiode. This change in laser position is fed back into the computer to generate the feedback loop which maintains a constant tip-surface distance and forms the 3D topographical maps produced

Samples must be firmly attached to not be susceptible to the friction and torsional forces placed upon them by the cantilever tip during scanning. The force applied is usually on the order of few tens of nN but varies with spring constants, and soft, biological samples are often not compatible with this imaging mode [4]. CM does present some advantages in that it can be readily modified to gain nanomechanical information or used with chemically modified cantilevers to provide chemical contrast on the sample [4]. In addition CM is the highest resolution form of AFM as it maintains contact with the sample surface throughout scanning.

Tapping Mode (TM)

This AFM mode is also known as “dynamic” or “intermittent contact” mode to reflect the movement of the cantilever during TM. In all these modes the cantilever is vibrated, and the amplitude, frequency or phase of this vibration is monitored. TM-AFM performed in ambient conditions involves using an oscillating cantilever near its resonance frequency, usually in order of 100–300 kHz, at an amplitude of 20–100 nm by means of the piezo built into the cantilever holder driving the oscillation (Fig. 2.3b), while work in a liquid environment typically requires a much softer cantilever, with a resonant frequency of approximately 30 kHz. With the advancement of underliquid imaging specialised cantilevers are now available which are ultra-short, and have resonant frequencies closer to that of traditional TM cantilevers [16]. The resonance frequency of the cantilever will depend on its dimensions and material properties, and is easily determined by sweeping through a range of frequencies to detect the response peak. A cantilever will usually have multiple resonance frequencies, but the strongest lowest natural frequency response is typically used for scanning. During the cantilevers oscillation it will “tap” into the

Fig. 2.3 This illustration shows the main AFM modes used in this work. **a** Contact mode AFM involves holding the cantilever in the repulsive regime at a set constant height above the sample while recording data on the topology and friction, using a feedback loop. **b** Tapping mode AFM oscillates the cantilever to reduce friction and the force applied to the sample. Phase data can also be collected to show a map of changes in the samples elasticity, **c** Ultrasonic force microscopy and **d** SThM; the cantilever is used as a heat sensor, with heat being applied using an AC current. Heat dissipation into the sample can be measured via the cantilever tip. **e** IR-AFM; a pulsed, tunable laser is focused onto the sample, and the IR-absorption of the sample leads to photothermal expansion. This expansion “kicks” the cantilever, leading to deflection and a measureable response



sample surface, and this contact creates a change in the resonance frequency and the amplitude of the cantilever. As the cantilever is being maintained at a constant set-point amplitude by the feedback loop (the same principle as during CM) the tip-surface distance is maintained. Any shifts in the amplitude are detected and

corrected by the feedback loop producing 3D image maps of the topographical features of the sample.

Phase TM imaging makes use of the specifics of tip-surface interactions which are not just topography dependent, but depend on characteristics such as elasticity, adhesion or hardness. Variations in these properties lead to a phase lag between the cantilevers oscillation and the signal being sent to the piezo driving the oscillation. The phase lag is recorded producing a 3D image map providing a qualitative map of the adhesion, and elastic moduli of the sample. Additionally, features such as sharp edges, which cannot be easily identified in the topography channel, can often be seen in phase, providing there is a difference between hardness and elasticity.

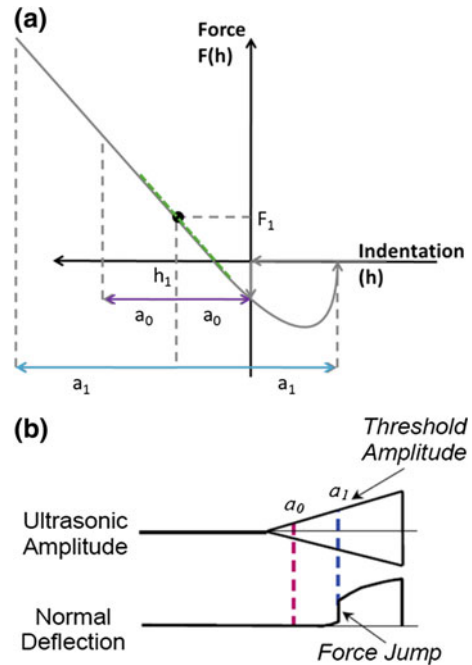
Non-contact modes like TM are particularly attractive for the imaging of biological samples due to the reduced friction placed on the sample. Data gathered in this manner will be discussed later (Sect. 6.2). TM AFM uses the cantilever in the border between attractive and repulsive regime, making use of VDWs forces, consequently a lower force (<1 pN) needs to be applied to maintain the regime.

Ultrasonic Force Microscopy (UFM)

UFM [20] was originally developed to overcome the limitations of the measuring the maximum measurable contact stiffness, which is usually determined by the cantilever's spring constant [5–7, 21]. Although an approximately spring constant is provided by the cantilevers manufacturer, should quantitative work been undertaken it is possible to accurately calculate a cantilevers spring constant using the Sader method. This method utilises the cantilever's resonant frequency and quality (Q) factor, (a measure of the dampening a resonator has), to determine the spring constant [22]. This variation of contact AFM allows qualitative [23, 24] and quantitative [25, 26] measurements of the elastic behaviour of a sample by oscillating the sample at frequencies f well above the cantilever resonant frequency f_0 (typically at $f = 2\text{--}10$ MHz compared to $f_0 = 10\text{--}300$ kHz). This out-of-plane vibration of the sample increases the effective cantilever's spring constant due to inertia [20]. In the context of UFM it is assume the cantilever does not vibrate at ultrasonic frequencies, and thus becomes “dynamically frozen” as the ultrasonic vibration of the sample is sufficiently high to prevent the cantilever responding to the sample surface motion. The cantilever's behaviour at this point makes it almost perfectly rigid due to this inertia, and allows the cantilever to indent briefly into the sample surface and pull away, thus probing the elastic properties of the sample surface (Fig. 2.3c [20]). The elastic indentation of the tip-sample can also be further modified by modulating the amplitude of the sample oscillation.

A vital component of UFM is the use of a piezo-transducer beneath the sample, which converts electrical energy into mechanical energy. By applying an electrical field to the piezo-ceramic disk attached to the metal stub AFM samples are held in place with an ultrasonic vibration can be applied directly to the sample in the z axis. The exposure of the ceramic to an AC field will cause it to cycle between expanding and contracting, at the cycling frequency of the field. By vibrating the piezo-ceramic between 2 and 4 MHz (close to its fundamental longitudinal

Fig. 2.4 **a** Typical force-versus-indentation curve. Tip-surface indentation is modulated using ultrasonic vibration at a set amplitude (a). A large enough amplitude (a_1) causes a force jump, seen in panel **b** as the tip leaves the sample surface. This force jump is detected as the deflection of the cantilever [5, 6, 29]



frequency) its spatial movement can be controlled. The frequency of the vibration applied is controlled tightly by the thickness of the piezo-ceramic used, as thinner disks respond to higher frequencies, and shape and composition can also influence the behaviour of piezo-ceramics.

The tip-surface interaction can be described using the force-versus-indentation curve (Fig. 2.4). As previously mentioned, when the cantilever tip is in close proximity to the sample surface, it experiences an attractive force followed by a repulsive one. As the tip retracts, it remains adhered to the sample surface until the pull-off distance is reached. In UFM an ultrasonic vibration (a) is applied to the sample. If this amplitude, a_0 , is small, the tip remains in contact with the sample surface for the full oscillation cycle, and the displacement of the sample is smaller than the initial indentation, so the average force, F , does not change (green line). When amplitude is increased to a_1 tip/sample contact is broken for part of the cycle, which creates additional force due to the nonlinearity of the force-versus-distance curve and hence the change in the average F_0 (grey line), which is otherwise known as the “force jump” [5, 6]. This is the threshold amplitude for the UFM, and the point at which the probe breaks free creates the “force jump” in the normal cantilever deflection.

The new force F_m can be calculated from the interaction force between sample and tip as follows:

$$F_m(h_1, \alpha) = \frac{1}{2\pi} \int_{T_{ul}} F(h_1 - \alpha \cos f_{ult} t) dt,$$

where $F(h)$ is the force dependence on the indentation depth without an out-of-plane ultrasonic vibration; f_{ult} is the ultrasonic frequency; the integral is taken over a period. $T_{ul} = 1/f_{ult}$. When F_m increases due to the non-linearity, the cantilever deflection increases as well until a new equilibrium position is reached. This new stationary normal deflection is given by:

$$F_m(h_{eq}, a) = k_c z_{eq},$$

where z_{eq} and h_{eq} are the new cantilever deflection and sample indentation depth, respectively and k_c is the cantilever stiffness constant.

This pull-off amplitude becomes the threshold amplitude for the system in use, and variations in it allow materials of different elastic properties to be contrasted as it is dependent on both elastic constant and adhesion hysteresis [7]. Adhesion hysteresis is defined as the difference between the work needed to break two surfaces apart compared to the work needed to bring them together [27, 28]. The elastic constant referred to here is the *Young's modulus*, and describes the tensile elasticity of an object, or its ability to deform along and axis when opposing force is applied. Further increases in the averaged force, F_u , leads to an increase of the average cantilever deflection z_0 by z_a , ultrasonic force deflection. As average deflection increases, it can be assumed that the equilibrium modulated indentation ($h_0 + a \cos 2\pi ft$) would decrease by the same amount of z_0 .

Variations in the threshold amplitude and force jump depend on the different elastic properties of the sample being scanned, and lead to variation in the ultrasonic deflection. In order to detect the deflection of the cantilever as a response of the sample the amplitude modulation frequency must be carefully chosen. It must be above the SPM cut-off frequency but below that of the cantilevers resonance and is usually between 0.5 and 3 kHz. In the case of this system the cut-off frequency was 2.3 kHz. If a value above is used, the cantilevers delay becomes comparable with the modulation period of the amplitude altering the UFM response. Below this frequency, the AFM feedback circuit modifies the ultrasonic deflection [7]. The deflection signal is fed into a lock-in using the modulation frequency signal as a reference, while the output from this lock-in amplifier becomes the UFM image. Another factor for consideration is the profile of the amplitude modulation used. A ramped (symmetrical saw toothed) profile was used throughout the work here but others have been tested. Incorrect selection can result in ambiguity in sample contrast and therefore material stiffness [5, 6].

The role of elasticity and adhesion in UFM

The force it takes to move one atom away from another, or to displace, is connected to the chemical bonds between atoms which determine the equilibrium position of one atom to another. This equilibrium position can be represented as directly proportional to the distance, $F = kx$, where F is the applied force, x is the deformation, and k the spring constant of the material in questions. This is otherwise known as Hooke's law and allows a deduction of the attractive and repulsive forces that govern atoms in an interatomic bond, and provides information about the force needed to break this bond. Hooke's law only describes a linear elastic deformation between bonds however, and caution should be taken when working with materials which have a non-linear relationship such as Silicon Carbide.

The behaviour of such force is linearly elastic and is usually the case for small displacements in most solid materials. However this is a simplified case and in reality the equilibrium position is effected by the forces imposed by neighbouring atoms and the characteristics of the sample [30].

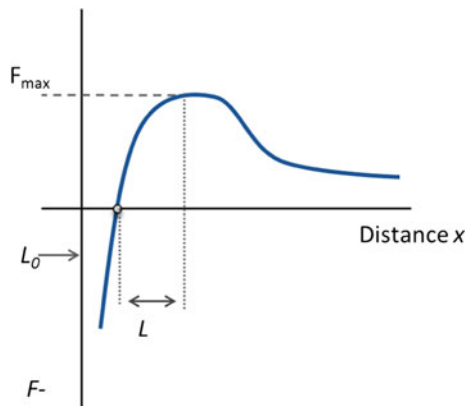
If one atom is pulled away from another Hooke's law provides the maximum value of force required to do so. This breaking of the chemical bond is known as the cohesive strength. After the bond is broken less and less force needs to be applied to keep the atoms separate. The bonds strength is equal to the max cohesive force (Fig. 2.5).

A force displacement curve can be approximated by a portion of a sine function [30] and the region between the equilibrium position and the max force is of most interest. Here

$$F = F_{max} \sin \frac{\pi x}{2L},$$

where L is the distance from the equilibrium position at F_{max} .

Fig. 2.5 The forces between an atom as part of a solid as it is pulled away from its equilibrium position. The short range interactions are governed by repulsive forces, while attractive forces act over a larger distance. F_{max} refers to the strength of the bond and the force necessary to break it. L is the distance from equilibrium position [30]



For small θ values $\sin \theta \approx \theta$, the force required for small displacements x is

$$F = F_{max} \sin \frac{\pi x}{2L}$$

$$F = \left[\frac{F_{max} \pi}{2L} \right] x$$

Values L and F_{max} can be considered constant for any one particular material, therefore it becomes $F = kx$ (Hooke's law). This can be extended to a force distributed over a unit area so that

$$\sigma = \frac{\sigma_{max} \pi}{2L} x,$$

where σ_{max} is the tensile strength of the material and the units of pressure.

If L_0 is the equilibrium distance then the strain ε for a given displacement x is defined as

$$\varepsilon = \frac{x}{L_0}$$

$$\text{Thus } \frac{\sigma}{\varepsilon} = \left[\frac{L_0 \pi \sigma_{max}}{2L} \right] = E$$

The terms in the square brackets are considered constant for any one particular material, and represent a single material property, E , the elastic modulus or Young's modulus of a material. This is another form of Hooke's law where stress is considered proportional to strain.

UFM can be used to discriminate between the elastic properties of materials by using this Young's modulus [6]. The Johnson–Kendal–Roberts [31] (JKR model) can be used to model the tip-surface interaction and adhesion hysteresis seen in UFM. In this model the contact area r_c between 2 spheres is given by

$$r_c^3 = \frac{3R}{4E_r} \left[F + 3\Delta\gamma\pi R + \left(6\Delta\gamma\pi R F + (3\Delta\gamma\pi R)^2 \right)^{\frac{1}{2}} \right],$$

where $\Delta\gamma$ is the Dupré work of adhesions, R is the tip radius on a perfectly flat surface, E_r is the reduced Young's modulus and F is the normal force being applied in the system.

Indentation depth h of the cantilever in a system is then calculated using:

$$h = \frac{r^2}{R^*} \left[1 - \frac{2}{3} \left(\frac{r_0}{r_c} \right) \right]^{\frac{3}{2}} \text{ is normalised to}$$

$$h_0 = \left(\frac{\Delta\gamma^2 \pi^2 R}{E_r^2} \right)^{\frac{1}{3}}$$

where the contact radius at zero normal force is r_0 and is equal to:

$$r_0^3 = 6\Delta\gamma \frac{\pi^2}{R^*} E_r$$

Which is normalised to $F_0 = \Delta\gamma\pi R$.

Materials that are more compliant have higher threshold amplitudes and adhesion hysteresis. This in turn will lead to an increased discontinuity at the pull-off point and subsequently the force jump of ultrasonic deflection. A more adhesive material will also have the same consequence. Simulations of the contact mechanics of UFM have shown that the threshold amplitude increases with increasing force, and also by reducing Young's modulus or increasing adhesions, and that the latter two factors will lead to an increase in the force jump detected by the system [5, 6]. It can therefore be difficult to distinguish between higher adhesion or increased compliance of a material, without additional information, such as friction behaviour. Topographical artefacts can also interfere with the adhesion properties of a material.

Caution should be taken with the above model of UFM as it can be considered over simplified. UFM as a technique is not without limitations; it does not take into consideration phase information and is therefore unsuitable for characterising materials with high viscoelastic properties (where indentation is time dependent) [5], surface topography and adhesion can affect quantitative analysis when performed (only the elastic properties of the sample and tip-sample interactions are considered by this model) [32], and thirdly adhesion forces are assumed to be uniform across the sample surface and contrast comes only from the change in the samples elastic properties, which can prove challenging for thin films or polymeric structures [5–7]. In addition any sharp changes in topography can affect the threshold amplitude and subsequent image contrast making the interpretation of the surface mechanical properties more challenging.

Scanning Thermal Microscopy

Scanning Thermal Microscopy (SThM) was originally developed in 1986 by combining STM with a thermal field to control the tip-sample height while probing the samples thermal properties [33, 34]. Several advances have occurred since the techniques initial development, reviewed extensively by Majumdar [35, 36]. The adaption of CM AFM used in this work allows the mapping of the local thermal properties of a sample by scanning the sample surface with a specially adapted cantilever which acts as a thermal sensor (Fig. 2.3d). As with all AFM techniques information is gained on nanometre scale resolution. Joule heating is used to heat the tip while in contact with the sample. Heat diffuses from tip to sample due to the temperature difference between them, and is proportional to the thermal conductivity of the sample and the tip. This subsequently changes the sensor temperature which is recorded as a change in the sensors electrical resistance, measured as the

current flowing into the electrical bridge. This current change is ultimately used to produce the thermal image.

The stationary diffusive heat transport equation is used to describe the heat transfer process in SThM,

$$\rho C_p \frac{\partial T}{\partial t} - \nabla(k \nabla T) = Q,$$

where p is the density of the material, C_p is the heat capacity, k is the thermal conductivity and Q is the heat source. In some samples there can be deviations from the diffusive heat transport model, such as at the end of the tip or in highly thermally conductive samples. In these samples the ballistic heat transport is significant and should be considered.

Heat flow into the sample is governed by the thermal resistance of the tip-sample contact, and is connected to the samples thermal conductivity, k . If the samples thermal conductivity is less than that of the probe then the measurements are dominated by the thermal conductivity of the sample [37]. Thermal conductivity is determined by the free path of phonons in the material, l , where

$$k = Cv l$$

and C is the specific heat and v the speed of sound in the sample. To calculate the temperature difference between the probe and sample ΔT and the heat flow (per unit time) ΔQ . Ultimately

$$\frac{\Delta Q}{\Delta T} = k_{sample} \pi R,$$

where R is the contact radius, which is pressure dependent.

The cantilever operation in SThM depends to a degree on the application it is being used for; thermomechanical data writing has very different needs to the nanoscale deposition of materials [38]. The application of SThM for the study of amyloid fibres is particularly useful and several studies have looked at the thermal properties of amyloid proteins during aggregation. Amyloid proteins by nature are display a high level of thermal stability, due to the thermodynamically favourable state of the aggregated form [39]. Dandurand et al. [40] recently showed the aggregation of a synthetic peptide, S4, could replicate that of amyloid fibres when under the correct conditions. Aggregation leads to an increase in thermal stability linked to the typical conformational change to a cross- β structure. Thermodynamic stability has also been linked to the folding and unfolding in Light Chain Amyloidosis [41]. Amyloid proteins have also been shown to undergo thermally induced melting, and unfold to their native conformations, a change which was not linked to their morphology [42].

Nanoscale infrared spectroscopy as an extension of Contact Mode AFM

A new extension of CM AFM involves combining IR spectroscopy techniques with an AFM cantilever as the nanoscale detector of the IR light absorption. This allows the optical diffraction limit of 10–30 μm to be overcome and provide spatial resolution on the order of 10–100 nm, and also overcoming a limit of AFM: the provision of chemical characterisation of a sample. This spatial resolution is improved upon compared to typical FTIR imaging, which is limited by the fundamental limit of twice the wavelength (10–30 μm) and also Attenuated Total Reflectance (ATR) which is limited by $\lambda/2$ (3–10 μm). In comparison Scanning Near-field IR Microscopy (SNIM) is also able to produce a resolution of 10–30 nm. IR-microspectroscopy allows the mapping of samples to produce a spatially resolved map of their chemical content.

AFM-IR was one of several techniques that resulted from the development of a tuneable Free Electron Laser (FEL) at CLIO (Centre Laser Infrarouge d'Orsay, Paris) [43] and showed the most promise for development. After consideration was given to the theoretical principles behind AFM-IR [44], the first experiments were conducted using the tuneable FEL teamed with an AFM to map the local transient deformations induced by IR light at sample specific wavelengths [9, 45, 46].

The principle of AFM-IR (Fig. 2.6) is simple, instead of a traditional laser light being shone onto the cantilever for detection of movement/mechanical responses of the sample, a pulsed, tuneable IR laser is used to illuminate the sample which is sat upon a ZnSe prism. This IR radiation will locally heat the sample via vibrational

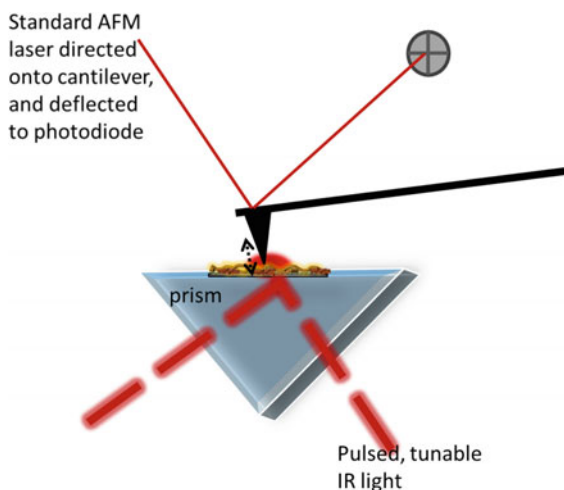


Fig. 2.6 The principle of Nano-IR. A pulsed and tuneable IR source is directed through a ZnSe prism, (from underneath), and onto the sample. The photothermal expansion of the sample “kicks” the cantilever, the movement of which is detected by a standard CM setup of a laser focused onto the cantilever and its deflection monitored. The ringdown of the cantilever produces the deflection, while its amplitude and absorption as a function of the wavelength can also be extracted

excitation of the sample molecules, which leads to rapid photothermal expansion of the sample. This local expansion is the result of the absorption of the IR radiation by the sample and its transmission through the sample by phonons within the sample lattice as a thermal wave. This occurs in a short pulse of expansion detected by the cantilever tip, (see Fig. 2.3e. for an overview of the cantilever detection). This pulse “kicks” the cantilever, and the ringdown of this kick can be measured, making it possible to extrapolate the amplitudes and oscillations of the ringdown for further analysis. In the case of the Nano-IR system developed by Anasys Instruments (Santa Barbara, USA) the IR absorption spectra which are obtained from the sample by measuring the photothermal expansion as a function of the wavelength of incident laser light. By tuning the laser to a specific absorption band the sample is then mapped for its photothermal response at that wavelength, but on the resolution level of the cantilever tip, not the optical diffraction limit. The sample stiffness can also be determined by studying the oscillation frequency of the cantilever ringdown. A thorough discussion of the details of the AFM-IR technique have been set out recently by Dazzi et al. [8]. This technique is reliant on exciting molecules via local heat absorption, and the propagation of the thermal waves this induces sample thickness is vital. The Nano-IR2 system can image samples approximately 20 nm thick but is optimal for samples 100–1000 nm thick, while thicker samples can be imaged with the original Nano-IR system. Detection of the IR induced thermal expansion is more challenging in samples whose thickness is on the order of microns.

The field of microspectroscopy is highly applicable to the study of biological samples, and the Nano-IR has proved to very popular in this respect. Selected areas of application are not limited to, but include, plants cells [47], lipids within the human cornea and hair [48, 49], pharmaceuticals [50], bone and other mineralised samples [51–53], cells [54] and also for detection of cancer biomarkers in a variety of cancers [55–58]. The most relevant application of AFM-IR to the work shown in this thesis is that conducted by Müller et al. [59]. A microstamp was used to deposit droplets of monomeric and aggregated lysozyme onto a ZnSe prism, and were able to differentiate between random coiled and β -sheets, which is a typical structural transition for amyloid proteins.

2.3 Dynamic Light Scattering (DLS)

Also sometimes referred to as Quasi-Elastic Light Scattering, DLS is an ideal technique for characterising particles in suspension in the sub-micron range. A highly sensitive technique it can readily be used to detect macromolecules such as proteins in solution.

In order to determine the size of a particle the Brownian motion of the particle can be measured. Particles such as proteins within a suspension are subject to random motion caused by interactions with the solvent molecules within the suspension. Brownian motion is linked to the size of the particle as larger particles are

influenced less by the solutes within the suspension, and move slower than smaller particles which are moved more rapidly. Two other important factors in accurately measuring the Brownian motion of a particle and thus determining its size are the temperature of the solution, and its viscosity. A stable temperature during measurement is essential to prevent random movements of the particles within the suspension. The speed at which a particle moves at is known as the translational diffusion coefficient (D).

Using D the hydrodynamic radius of a particle can be calculated via the Stokes-Einstein equation;

$$d(H) = \frac{kT}{3\pi\eta D}$$

where $d(H)$ the hydrodynamic diameter, k the Boltzmann's constant, T the absolute temperature and η the viscosity. The Stokes-Einstein equation assumes that the particle being measured is spherical, so caution must be used when measuring larger, fibril like particles whose dimensions are not spherical. Determining the hydrodynamic radius of a particle is also influenced by any surface structures on the particle, such as charged residues, which may affect its diffusion speed.

In order to collect data on the particles size as a function of its translational diffusion, DLS, as its name suggests, involves collecting information on the scattering of light by the particles in a solution. Typically a HeNe laser is used to create this scattering by illuminating the sample. Depending on the scattering angle data is either collected using forward or back scattering light. Back-scatter has significant advantages over forward scattering, as the light does not have to completely penetrate the sample, removing any conflicting scattered light from neighboring particles. Time dependent fluctuations in the scattered light are measured using a fast photon counter [60] In addition, large contaminants like dust particles typically scatter light forwards and are therefore not likely to be detected. Larger particles will scatter light further and with greater intensity than smaller ones, and also obscure any nearby smaller particles scattered light, leading to a misrepresentation of the sample contents. Larger particles move much slower than smaller ones, due to the greater effects of Brownian motion upon them, and also scatter light further due their increased size (the scattering of light is proportional to the sixth power of its diameter from Rayleigh's approximation). Smaller particles conversely will scatter light with faster intensity fluctuations, as this is connected to the speed of the particles in motion. Factors such as sample concentration can also affect the signal detected using DLS, as more concentrated samples will behave in a manner similar to large particles, in that they will scatter more light and swamp the signal of neighboring particles.

DLS has been used to great success to study the aggregation of A β 1:42, both alone and with potential pharmaceutical interactions [61–64]. One study has shown that A β 1:40 samples can initially be detected at ~ 7 nm in size and monodispersed, indicating a uniform population structure. As aggregation persisted this population became more polydispersed as aggregates ranging from 10 to 52 nm in size were

detected. Larger aggregates at later time points, more akin to fibrils were not detected by DLS, but detectable by Multi-angle Light Scattering [65–67]. In contrast the monomeric form of A β 1:42 is 1–2 nm in diameter [68, 69]. Cizas et al. (2010) noted that A β 1:42 monomer size is particularly sensitive to different preparations, or deseeding techniques. Pretreatment of A β 1:42 with HFIP produced monomers \sim 2 nm in size, while agitation of this sample produced monomers of 8 nm in size. This technique has also been used to monitor the effect of metal ions, and their chelators, on A β 1:42 aggregation and for complex studies of aggregation kinetics [70]. It is therefore possible to use DLS to monitor the temporal change in aggregate sizes of A β 1:40/2. A disadvantage of DLS is that no details of the population sizes i.e. monomer/dimer/trimer can be determined. It is for this reason DLS is best used in conjunction with other techniques, such as AFM [68, 69] or ThT [70].

2.4 Direct Imaging via AFM and Electron Microscopy Studies of A β 1:42 and Their Findings

The pathology of AD and aggregation process of the main pathogenic component of the disease, A β , will be discussed in more detail in Chapter Three. Here we will focus purely on the information about A β which has been gained from the application of physical techniques, most notably cryo-EM, STM and AFM.

It has been over a decade since A β was first imaged using AFM; in 1999 Blackley et al. [71] successfully imaged A β 1:40 and followed the aggregation of the peptide using TM AFM. Immediately after wetting the peptide was visible as small spherical aggregates, before fibrillisation commenced. Fibrillisation took the form of the spherical aggregates interacting to become short fibrillary structures which later elongated, occasionally becoming branched structures. The detection of a period twist of approximately 25 nm on some mature A β fibres was also an important discovery. In addition the transient nature of oligomeric units of A β was noted.

The first time point noted using an AFM, and most crucial for studies of pharmaceutical and neurotoxic behaviours, are the early aggregates. Several studies have confirmed the monomer has a spherical appearance and is approximately 2 nm in size [68, 69, 71, 72], which correlates well with DLS and other techniques. Dimers of A β are typically around 4 nm in size and maintain an elliptical state [72].

Morphological differences between the two main isoforms of A β can be detected at later stages of aggregation; A β 1:40 protofibrils are smaller than A β 1:42, (3.1 ± 0.31 nm compared to 4.2 ± 0.58 nm), however both forms of protofibrils were typically 50–200 nm long and curved in appearance [73, 74]. The difference in widths of the two protofibrillar isoforms can be attributed to the additionally amino acid residues in A β 1:42 [73]. Later aggregates have been classified further with the aid of AFM to be either type I (\sim 5 nm high, 600 nm long [73–76]) or type

II structures. Type II fibres are longer, ($>1\ \mu\text{m}$), between 6 and 13 nm wide, and often have a branched or junctional morphology [73, 77, 78]. Type II fibrils are the mature fibres produced after several protofibrils have elongated, interacted and twisted together [77].

A β fibres are highly polymorphic in nature due to the stacking nature of the β -sheets, and their morphology can be surface dependent. A β 1:42 deposited onto Highly Ordered Pyrolytic Graphene (HOPG) forms ribbon like protofibrils as opposed to cylindrical ones on mica [81] while positively and negatively charged surfaces have different effects on aggregation. Adjusting the surface of the substrate to become more hydrophobic by CH_3 modification leads to the formation of spherical and amorphous aggregates which cluster together in a dense surface covering, and while surfaces modified with COOH or NH_2 also showed an initial covering of spherical aggregates $\sim 2\ \text{nm}$ high, these elongated rapidly into mature fibres [82]. It was proposed that the hydrophobic surface promoted the formation of alpha helix dominated aggregates, while charged surfaces will interact with the charged regions within A β leading to the promotion of β -sheets, and therefore fibre formation [82]. The periodicity of the twist often seen on amyloid fibres can also be affected by the surface the protein is deposited onto, or aggregated on. A right handed helical periodicity has been noted for deposition on HOPG [83] while hydrophilic surfaces lead to a left handed helix forming [73, 75].

One of the most significant features of amyloid fibres for which evidence is hard to gather is that of the substructure. It is well established that mature amyloid fibres are made of multiple protofibrils, or elongated protofilaments, twisted together, but debate still exists about the exact number which occur in A β 1:40/2 and the substructure that their interaction creates. Imaging of MF by TEM has shown that A β fibres have a polarity or directionality to their structure [84]. It has been suggested from STM images of MF of A β 1:42 that these fibres are made of 1 or 2 intertwining protofilaments [75, 80, 85, 86], each of which is made of two protofibrils with its own has a cross- β structure [87, 88]. A hollow core within the MF was been detected by EM in 1986 [86] and numerous times with STM, but not AFM [83, 89, 90] (Fig. 1.7). Recently it has been proposed that the internal structure of A β 1:42 is composed of two peripheral regions surrounding a central core, which itself has a region of lower density and two higher density packed cores [80, 84, 85]. Cryo-EM techniques have so far proven to show the most detailed information about A β internal structure and morphology, and the higher density regions have been linked directly to the hairpin turn produced by the β -sheets [85]. More importantly differences between the morphology of A β 1:40 and 1:42 have been noted using cryo-EM and STM. The central hollow core seen in A β 1:42 is lacking in A β 1:40, with the higher density region extending the whole cross section of the fibre [85]. This increased width for A β 1:40 MF indicates that the high density regions are composed of more β -hairpins than the longer isoform, potentially indicating that A β 1:40 is made of 2 intertwining protofilaments, each made of 2 protofibrils [84, 85] (Fig. 2.7). However multiple reconstructions of the A β 1:40 MF indicate different structures suggesting that incubation conditions, sample preparation, substrate deposition and numerous other factors could all affect the structure ultimately

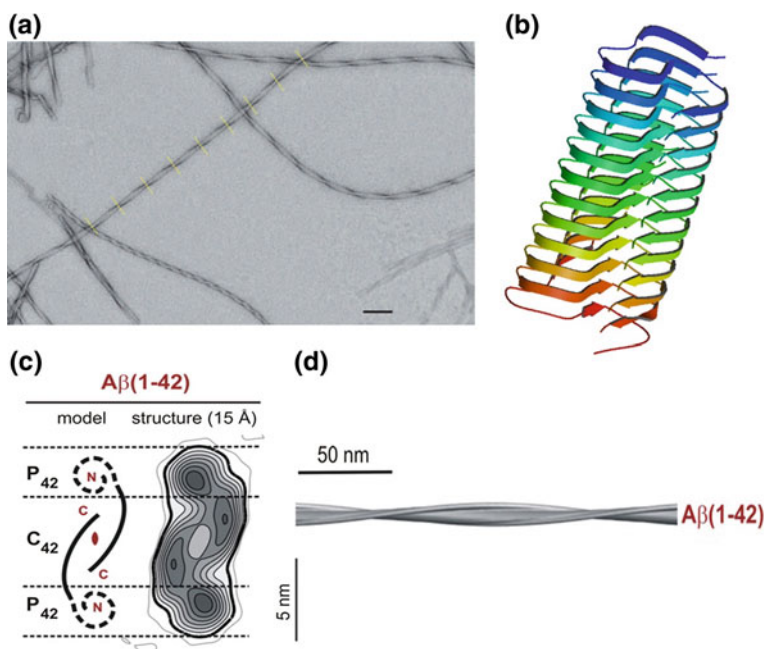


Fig. 2.7 The structure of A β fibres. **a** EM imaging of A β 1:40 fibres reveals a two protofilament structure periodicity, with the twist indicated by the yellow line [79]. **b** Solid state NMR data suggests A β 1:42 has a triple β sheet motif with hairpin turns surrounding a central core [29]. **c, d** Advanced cryo-EM work suggests reveals the structure of the protofilaments within a fibre: A β 1:42 is made of two peripheral regions surrounding a central core, which itself has a region of lower density and two higher density packed cores [79, 80]

formed. Models have proposed anything from 2 to 3 protofilaments interact together to produce the MF [80, 91, 92], with multiple morphologies within the same sample possible due to differences in inter- and intra-residue interactions [92].

2.5 Conclusion

Here we have discussed the key physical techniques employed in this thesis to study A β 1:42 during its aggregation. Multiple modes of SPM have been employed. While TM is the most commonly used AFM mode for imaging biological samples it fails to offer any insights into chemical, thermal or nanomechanical properties. These insights can be gained by employing adaptations of CM AFM to produce techniques such as UFM, SThM and AFM-IR (commercially available as the Nano-IR system). The differences between the data which can be gathered by these techniques has been discussed above. In addition mention is given to DLS, which

can offer detailed analysis of particle sizes and population dynamics over the aggregation timecourse.

In order to understand more about the morphological behaviour and structural details of biological materials it is necessary to move beyond modelling their structures based on computational techniques, and study their aggregation in reality. Techniques such as EM, STM and AFM allow one to see a snapshot of the aggregation state of peptides like A β 1:42, and make connections with the theoretical models. AFM and cryo-EM have provided a detailed image of what the MF of A β looks like, and how it forms. When used in conjunction with techniques such as FTIR (or other spectroscopy methods) or DLS applications commonly applied elsewhere can provide a powerful arsenal for the study of amyloid peptide aggregation.

References

1. Binnig, G., Quate, C. F., & Gerber, C. (1986). Atomic force microscope. *Physical Review Letters*, 56, 930–933.
2. Binnig, G., & Rohrer, H. (1982). Scanning tunneling microscopy. *Helvetica Physica Acta*, 55, 726–735.
3. Binnig, G., Rohrer, H., Gerber, C., & Weibel, E. (1982). Tunneling through a controllable vacuum gap. *Applied Physics Letters*, 40, 178–180.
4. Jandt, K. D. (2001). Atomic force microscopy of biomaterials surfaces and interfaces. *Surface Science*, 491, 303–332.
5. Dinelli, F., Biswas, S. K., Briggs, G. A. D., & Kolosov, O. V. (2000). Measurements of stiff-material compliance on the nanoscale using ultrasonic force microscopy. *Physical Review B*, 61, 13995–14006.
6. Dinelli, F., et al. (2000). Mapping surface elastic properties of stiff and compliant materials on the nanoscale using ultrasonic force microscopy. *Philosophical Magazine A Physics of Condensed Matter Structure Defects and Mechanical Properties*, 80, 2299–2323.
7. Dinelli, F., Assender, H. E., Takeda, N., Briggs, G. A. D., & Kolosov, O. V. (1999). Elastic mapping of heterogeneous nanostructures with ultrasonic force microscopy (UFM). *Surface and Interface Analysis*, 27, 562–567.
8. Dazzi, A., et al. (2012). AFM-IR: Combining atomic force microscopy and infrared spectroscopy for nanoscale chemical characterization. *Applied Spectroscopy*, 66, 1365–1384.
9. Dazzi, A., Prazeres, R., Glotin, E., & Ortega, J. M. (2005). Local infrared microspectroscopy with subwavelength spatial resolution with an atomic force microscope tip used as a photothermal sensor. *Optics Letters*, 30, 2388–2390.
10. Marcott, C., et al. (2012). Nanoscale IR spectroscopy: AFM-IR—A new technique. *Spectroscopy*, 27, 60–65.
11. Tovee, P. D., & Kolosov, O. V. (2013). Mapping nanoscale thermal transfer in-liquid environment-immersion scanning thermal microscopy. *Nanotechnology*, 24.
12. Tovee, P. D., et al. (2014). Nanoscale resolution scanning thermal microscopy using carbon nanotube tipped thermal probes. *Physical Chemistry Chemical Physics*, 16, 1174–1181.
13. Tovee, P., Pumarol, M., Zeze, D., Kjoller, K., & Kolosov, O. (2012). Nanoscale spatial resolution probes for scanning thermal microscopy of solid state materials. *Journal of Applied Physics*, 112.

14. Gandyra, D., Walheim, S., Gorb, S., Barthlott, W., & Schimmel, T. (2015). The capillary adhesion technique: A versatile method for determining the liquid adhesion force and sample stiffness. *Beilstein Journal of Nanotechnology*, 6, 11–18.
15. Weisenhorn, A. L., Hansma, P. K., Albrecht, T. R., & Quate, C. F. (1989). Forces in atomic force microscopy in air and water. *Applied Physics Letters*, 54, 2651–2653.
16. Baro, A. M. R. R. G. (Eds.). (2012). Wiley-VCH.
17. DoITPoMS. (2013). *Teaching and learning package*. University of Cambridge. http://www.doitpoms.ac.uk/tlplib/afm/tip_surface_interaction.php. Accessed February 24, 2015.
18. Bonnell, D. (2001). *Scanning probe microscopy and spectroscopy: Theory, techniques, and applications*. New York, USA: Wiley-Blackwell.
19. Eaton, P. W. P. (2010). *Atomic force microscopy*. Oxford: Oxford University Press.
20. Kolosov, O. V., & Yamanaka, K. (1993). Nonlinear detection of ultrasonic vibrations in an atomic force microscope. *Japanese Journal of Applied Physics Part 2-Letters*, 32, L1095–L1098.
21. Dinelli, F., Biswas, S. K., Briggs, G. A. D., & Kolosov, O. V. (1997). Ultrasound induced lubricity in microscopic contact. *Applied Physics Letters*, 71, 1177–1179.
22. Sader, J. E., Chon, J. W. M., & Mulvaney, P. (1999). Calibration of rectangular atomic force microscope cantilevers. *Review of Scientific Instruments*, 70, 3967–3969.
23. Robinson, B. J., Kay, N. D., & Kolosov, O. V. (2013). Nanoscale interfacial interactions of graphene with polar and nonpolar liquids. *Langmuir*, 29, 7735–7742.
24. Robinson, B. J., et al. (2014). Nanomechanical mapping of graphene layers and interfaces in suspended graphene nanostructures grown via carbon diffusion. *Thin Solid Films*, 550, 472–479.
25. Robinson, B. J., & Kolosov, O. V. (2014). Probing nanoscale graphene-liquid interfacial interactions via ultrasonic force spectroscopy. *Nanoscale*, 6, 10806–10816.
26. Bosse, J. L., Tovee, P. D., Huey, B. D., & Kolosov, O. V. (2014). Physical mechanisms of megahertz vibrations and nonlinear detection in ultrasonic force and related microscopies. *Journal of Applied Physics*, 115.
27. Chaudhury, M. K., & Owen, M. J. (1993). Adhesion hysteresis and friction. *Langmuir*, 9, 29–31.
28. Wei, Z., He, M.-F., & Zhao, Y.-P. (2010). The effects of roughness on adhesion hysteresis. *Journal of Adhesion Science and Technology*, 24, 1045–1054.
29. Xiao, Y., & Ma, B. (2015). Abeta(1–42) fibril structure illuminates self-recognition and replication of amyloid in Alzheimer’s disease.
30. Fischer-Cripps, A. C. (2007). *Introduction to contact mechanics*. New York: Springer.
31. Johnson, K. L., Kendall, K., & Roberts, A. D. (1971). Surface energy and contact of elastic solids. *Proceedings of the Royal Society of London Series A Mathematical and Physical Sciences*, 324, 301.
32. Rabe, U., Janser, K., & Arnold, W. (1996). Vibrations of free and surface-coupled atomic force microscope cantilevers: Theory and experiment. *Review of Scientific Instruments*, 67, 3281–3293.
33. Rajakarunanayake, Y. N., & Wickramasinghe, H. K. (1986). Nonlinear photothermal imaging. *Applied Physics Letters*, 48, 218–220.
34. Williams, C. C., & Wickramasinghe, H. K. (1986). Scanning thermal profiler. *Applied Physics Letters*, 49, 1587–1589.
35. Igeta, M., Inoue, T., Varesi, J., & Majumdar, A. (1999). Thermal expansion and temperature measurement in a microscopic scale by using the atomic force microscope. *JSME International Journal Series B Fluids and Thermal Engineering*, 42, 723–730.
36. Majumdar, A., Carrejo, J. P., & Lai, J. (1993). Thermal imaging using the atomic force microscope. *Applied Physics Letters*, 62, 2501–2503.
37. Fischer, H. (2005). Quantitative determination of heat conductivities by scanning thermal microscopy. *Thermochimica Acta*, 425, 69–74.
38. Lee, J., et al. (2006). Electrical, thermal, and mechanical characterization of silicon microcantilever heaters. *Journal of Microelectromechanical Systems*, 15, 1644–1655.

39. Gazit, E. (2002). The “Correctly folded” state of proteins: Is it a metastable state. *Angewandte Chemie-International Edition*, 41, 257.
40. Dandurand, J., et al. (2014). Conformational and thermal characterization of a synthetic peptidic fragment inspired from human tropoelastin: Signature of the amyloid fibers. *Pathologie Biologie*, 62, 100–107.
41. Blancas-Mejia, L. M., et al. (2014). Kinetic control in protein folding for light chain amyloidosis and the differential effects of somatic mutations. *Journal of Molecular Biology*, 426, 347–361.
42. Morel, B., Varela, L., & Conejero-Lara, F. (2010). The thermodynamic stability of amyloid fibrils studied by differential scanning calorimetry. *Journal of Physical Chemistry B*, 114, 4010–4019.
43. Ortega, J. M., Glotin, F., & Prazeres, R. (2006). Extension in far-infrared of the CLIO free-electron laser. *Infrared Physics & Technology*, 49, 133–138.
44. Dazzi, A., Goumri-Said, S., & Salomon, L. (2004). Theoretical study of an absorbing sample in infrared near-field spectromicroscopy. *Optics Communications*, 235, 351–360.
45. Dazzi, A., Prazeres, R., Glotin, F., & Ortega, J. M. (2007). Analysis of nano-chemical mapping performed by an AFM-based (“AFMIR”) acousto-optic technique. *Ultramicroscopy*, 107, 1194–1200.
46. Dazzi, A., Prazeres, R., Glotin, F., & Ortega, J. M. (2006). Subwavelength infrared spectromicroscopy using an AFM as a local absorption sensor. *Infrared Physics & Technology*, 49, 113–121.
47. Wolkers, W. F., Oldenhof, H., Alberda, M., & Hoekstra, F. A. (1998). A fourier transform infrared microspectroscopy study of sugar glasses: Application to anhydrobiotic higher plant cells. *Biochimica Et Biophysica Acta-General Subjects*, 1379, 83–96.
48. Marcott, C., et al. (2013). Nanoscale infrared (IR) spectroscopy and imaging of structural lipids in human stratum corneum using an atomic force microscope to directly detect absorbed light from a tunable IR laser source. *Experimental Dermatology*, 22, 419–421.
49. Marcott, C., et al. (2014). Localization of human hair structural lipids using nanoscale infrared spectroscopy and imaging. *Applied Spectroscopy*, 68, 564–569.
50. Van Eerdenbrugh, B., Lo, M., Kjoller, K., Marcott, C., & Taylor, L. S. (2012). Nanoscale mid-infrared imaging of phase separation in a drug-polymer blend. *Journal of Pharmaceutical Sciences*, 101, 2066–2073.
51. Paschalis, E. P., Betts, F., DiCarlo, E., Mendelsohn, R., & Boskey, A. L. (1997). FTIR microspectroscopic analysis of normal human cortical and trabecular bone. *Calcified Tissue International*, 61, 480–486.
52. Paschalis, E. P., Betts, F., DiCarlo, E., Mendelsohn, R., & Boskey, A. L. (1997). FTIR microspectroscopic analysis of human iliac crest biopsies from untreated osteoporotic bone. *Calcified Tissue International*, 61, 487–492.
53. Mendelsohn, R., Paschalis, E. P., & Boskey, A. L. (1999). Infrared spectroscopy, microscopy, and microscopic imaging of mineralizing tissues: Spectra-structure correlations from human iliac crest biopsies. *Journal of Biomedical Optics*, 4, 14–21.
54. Lasch, P., Boese, M., Pacifico, A., & Diem, M. (2002). FT-IR spectroscopic investigations of single cells on the subcellular level. *Vibrational Spectroscopy*, 28, 147–157.
55. Wood, B. R., et al. (1998). FTIR microspectroscopic study of cell types and potential confounding variables in screening for cervical malignancies. *Biospectroscopy*, 4, 75–91.
56. Lasch, P., Haensch, W., Lewis, E. N., Kidder, L. H., & Naumann, D. (2002). Characterization of colorectal adenocarcinoma sections by spatially resolved FT-IR microspectroscopy. *Applied Spectroscopy*, 56, 1–9.
57. Lasch, P., Haensch, W., Naumann, D., & Diem, M. (2004). Imaging of colorectal adenocarcinoma using FT-IR microspectroscopy and cluster analysis. *Biochimica Et Biophysica Acta-Molecular Basis of Disease*, 1688, 176–186.
58. Mordechai, S., et al. (2004). Possible common biomarkers from FTIR microspectroscopy of cervical cancer and melanoma. *Journal of Microscopy-Oxford*, 215, 86–91.

59. Müller, T., et al. (2014). Nanoscale spatially resolved infrared spectra from single microdroplets. *Lab on a Chip*, 14, 1315–1319.
60. Pryor, N. E., Moss, M. A., & Hestekin, C. N. (2012). Unraveling the early events of amyloid-beta protein (A beta) aggregation: Techniques for the determination of A beta aggregate size. *International Journal of Molecular Sciences*, 13, 3038–3072.
61. Loureiro, J. A., Gomes, B., Coelho, M. A. N., Pereira, M. D., & Rocha, S. (2014). Targeting nanoparticles across the blood-brain barrier with monoclonal antibodies. *Nanomedicine*, 9, 709–722.
62. Yang, Z. Z., et al. (2013). Enhanced brain distribution and pharmacodynamics of rivastigmine by liposomes following intranasal administration. *International Journal of Pharmaceutics*, 452, 344–354.
63. Salvati, E., et al. (2013). Liposomes functionalized to overcome the blood-brain barrier and to target amyloid-beta peptide: The chemical design affects the permeability across an in vitro model. *International Journal of Nanomedicine*, 8.
64. Gobbi, M., et al. (2010). Lipid-based nanoparticles with high binding affinity for amyloid-beta (1–42) peptide. *Biomaterials*, 31, 6519–6529.
65. Carrota, R., Manno, M., Bulone, D., Martorana, V., & San Biagio, P. L. (2005). Protofibril formation of amyloid beta-protein at low pH via a non-cooperative elongation mechanism. *Journal of Biological Chemistry*, 280, 30001–30008.
66. Lomakin, A., Chung, D. S., Benedek, G. B., Kirschner, D. A., & Teplow, D. B. (1996). On the nucleation and growth of amyloid beta-protein fibrils: Detection of nuclei and quantitation of rate constants. *Proceedings of the National Academy of Sciences of the United States of America*, 93, 1125–1129.
67. Lomakin, A., Teplow, D. B., Kirschner, D. A., & Benedek, G. B. (1997). Kinetic theory of fibrillogenesis of amyloid beta-protein. *Proceedings of the National Academy of Sciences of the United States of America*, 94, 7942–7947.
68. Cizas, P., et al. (2010). Size-dependent neurotoxicity of beta-amyloid oligomers. *Archives of Biochemistry and Biophysics*, 496, 84–92.
69. Parbhu, A., Lin, H., Thimm, J., & Lal, R. (2002). Imaging real-time aggregation of amyloid beta protein (1–42) by atomic force microscopy. *Peptides*, 23, 1265–1270.
70. Streets, A. M., Sourigues, Y., Kopito, R. R., Melki, R., & Quake, S. R. (2013). Simultaneous measurement of amyloid fibril formation by dynamic light scattering and fluorescence reveals complex aggregation kinetics. *PloS One*, 8.
71. Blackley, H. K. L., et al. (1999). Morphological development of beta(1–40) amyloid fibrils. *Experimental Neurology*, 158, 437–443.
72. Roher, A. E., et al. (2000). Oligomerization and fibril assembly of the amyloid-beta protein. *Biochimica Et Biophysica Acta-Molecular Basis of Disease*, 1502, 31–43.
73. Harper, J. D., Wong, S. S., Lieber, C. M., & Lansbury, P. T. (1997). Observation of metastable A beta amyloid protofibrils by atomic force microscopy. *Chemistry & Biology*, 4, 119–125.
74. Walsh, D. M., Lomakin, A., Benedek, G. B., Condron, M. M., & Teplow, D. B. (1997). Amyloid beta-protein fibrillogenesis—Detection of a protofibrillar intermediate. *Journal of Biological Chemistry*, 272, 22364–22372.
75. Harper, J. D., Wong, S. S., Lieber, C. M., & Lansbury, P. T. (1999). Assembly of A beta amyloid protofibrils: An in vitro model for a possible early event in Alzheimer's disease. *Biochemistry*, 38, 8972–8980.
76. Walsh, D. M., et al. (1999). Amyloid beta-protein fibrillogenesis—Structure and biological activity of protofibrillar intermediates. *Journal of Biological Chemistry*, 274, 25945–25952.
77. Serem, W. K., Bett, C. K., Ngunjiri, J. N., & Gamo, J. C. (2011). Studies of the growth, evolution, and self-aggregation of beta-amyloid fibrils using tapping-mode atomic force microscopy. *Microscopy Research and Technique*, 74, 699–708.
78. Gosal, W. S., Clark, A. H., & Ross-Murphy, S. B. (2004). Fibrillar beta-lactoglobulin gels: Part 1. Fibril formation and structure. *Biomacromolecules*, 5, 2408–2419.
79. Fändrich, M., Schmidt, M., & Grigorieff, N. (2011). Recent progress in understanding Alzheimer's β -amyloid structures. *Trends in Biochemical Sciences*, 36, 338–345.

80. Schmidt, M., et al. (2009). Comparison of Alzheimer A β (1–40) and A β (1–42) amyloid fibrils reveals similar protofilament structures. *Proceedings of the National Academy of Sciences of the United States of America*, 106, 19813–19818.
81. Arimon, M., et al. (2005). Fine structure study of A beta(1–42) fibrillogenesis with atomic force microscopy. *FASEB Journal*, 19, 1344.
82. Moores, B., Drolle, E., Attwood, S. J., Simons, J., & Leonenko, Z. (2011). Effect of surfaces on amyloid fibril formation. *PLoS ONE*, 6, 8.
83. Wang, Z. G., et al. (2003). AFM and STM study of beta-amyloid aggregation on graphite. *Ultramicroscopy*, 97, 73–79.
84. Fändrich, M., Schmidt, M., & Grigorieff, N. (2011). Recent progress in understanding Alzheimer's β -amyloid structures. *Trends in Biochemical Sciences*, 36, 338–345.
85. Zhang, R., et al. (2009). Interprotofilament interactions between Alzheimer's A beta(1–42) peptides in amyloid fibrils revealed by cryoEM. *Proceedings of the National Academy of Sciences of the United States of America*, 106, 4653–4658.
86. Miyakawa, T., Watanabe, K., & Katsuragi, S. (1986). Ultrastructure of amyloid fibrils in Alzheimers-disease and downs-syndrome. *Virchows Archiv B Cell Pathology Including Molecular Pathology*, 52, 99–106.
87. Serpell, L. C. (2000). Alzheimer's amyloid fibrils: Structure and assembly. *Biochimica Et Biophysica Acta-Molecular Basis of Disease*, 1502, 16–30.
88. Serpell, L. C., et al. (1995). Examination of the structure of the transthyretin amyloid fibril by image-reconstruction from electron-micrographs. *Journal of Molecular Biology*, 254, 113–118.
89. Miller, Y., Ma, B. Y., Tsai, C. J., & Nussinov, R. (2010). Hollow core of Alzheimer's A beta (42) amyloid observed by cryoEM is relevant at physiological pH. *Proceedings of the National Academy of Sciences of the United States of America*, 107, 14128–14133.
90. Miller, Y., Ma, B. Y., & Nussinov, R. (2011). The unique Alzheimer's beta-amyloid triangular fibril has a cavity along the fibril axis under physiological conditions. *Journal of the American Chemical Society*, 133, 2742–2748.
91. Sachse, C., et al. (2006). Quaternary structure of a mature amyloid fibril from Alzheimer's A beta(1–40) peptide. *Journal of Molecular Biology*, 362, 347–354.
92. Meinhardt, J., Sachse, C., Hortschansky, P., Grigorieff, N., & Fandrich, M. (2009). A beta(1–40) fibril polymorphism implies diverse interaction patterns in amyloid fibrils. *Journal of Molecular Biology*, 386, 869–877.

Nanoscale Imaging and Characterisation of Amyloid- β

Tinker-Mill, C.L.

2016, XX, 149 p. 59 illus., 14 illus. in color., Hardcover

ISBN: 978-3-319-39533-3